

A hybrid multi resolution scheme to efficiently model the structure of reionization on the largest scales

Han-Seek Kim^{1*}, J. Stuart B. Wyithe^{1,2}, Jaehong Park¹, Gregory B. Poole¹,
C. G. Lacey³, and C. M. Baugh³

¹*School of Physics, The University of Melbourne, Parkville, VIC 3010, Australia*

²*ARC Centre of Excellence for All-sky Astrophysics (CAASTRO)*

³*Institute for Computational Cosmology, Department of Physics, University of Durham, South Road, Durham DH1 3LE, UK*

ABSTRACT

Redshifted 21cm measurements of the structure of ionised regions that grow during reionization promise to provide a new probe of early galaxy and structure formation. One of the challenges of modelling reionization is to account both for the sub-halo scale physics of galaxy formation and the regions of ionization on scales that are many orders of magnitude larger. To bridge this gap we first calculate the statistical relationship between ionizing luminosity and Mpc-scale overdensity using detailed models of galaxy formation computed using relatively small volume - ($\sim 100\text{Mpc}/h$)³, high resolution dark matter simulations. We then use a Monte-Carlo technique to apply this relationship to reionization of the intergalactic medium within large volume dark matter simulations - ($>1\text{Gpc}/h$)³. The resulting simulations can be used to address the contribution of very large scale clustering of galaxies to the structure of reionization, and show that volumes larger than $500\text{Mpc}/h$ are required to probe the largest reionization features mid-way through reionization. As an example application of our technique, we demonstrate that the predicted 21cm power spectrum amplitude and gradient could be used to determine the importance of supernovae feedback for early galaxy formation.

Key words: Cosmology: theory; diffuse radiation; dark ages, reionization, first stars; Galaxies: high-redshift

1 INTRODUCTION

A new generation of radio telescopes including LOFAR¹ (Low Frequency Array), MWA² (Murchison Widefield Array), and PAPER³ (Precision Array for Probing the Epoch of Reionization) hope to observe the evolution of neutral hydrogen during the reionization of the Universe. The resulting measurements of the timing and structure of reionization promise to probe the properties of the first galaxies (Barkana & Loeb 2001; Pen et al. 2009; Mesinger et al. 2011; Ahn et al. 2012).

Theoretical modelling suggests that on large scales overdense regions are reionized first due to galaxy bias (Ciardi et al. 2003; Furlanetto et al. 2004b,a; Wyithe & Morales 2007; Iliev et al. 2007; Zahn et al. 2007; McQuinn et al. 2007; Trac et al. 2008). The size and evolution of HII re-

gions is therefore sensitive to the process of galaxy formation because the distribution of ionizing photons relative to the density field depends on the typical halo mass of star forming galaxies. For example, there has been a range of studies which show that reionization can be self-regulating (Dijkstra et al. 2004; Iliev et al. 2007; Mesinger & Dijkstra 2008; Ahn et al. 2012) because low mass galaxies are suppressed in a heated IGM. Supernova feedback also plays a significant role in the history and structure of reionization by suppressing star formation in lower mass halos (Wyithe & Loeb 2013; Kim et al. 2013).

Simulations of large volumes of the IGM during reionization are important for interpreting upcoming observational programs with the MWA and LOFAR because of their large field of view, which correspond to several Gpc at $z > 6$. In addition, large volume simulations are essential for testing of convergence of reionization properties (Iliev et al. 2013). However, until very recently, the largest simulations that include physical modelling of galaxy formation had a box size of $\sim 100\text{Mpc}$ (Kim et al. 2013; Norman et al. 2013; Gnedin 2014; Genel et al. 2014). Larger volumes have

* hansikk@unimelb.edu.au

¹ <http://lofar.org>

² <http://haystack.mit.edu/arrays/MWA>

³ <http://eor.berkeley.edu>

generally employed fully semi-numerical schemes or radiative transfer based on simple source models for the relationship between the ionizing luminosity and host dark matter halo mass (Santos et al. 2010; Mesinger et al. 2011; Iliev et al. 2013). Recently, Battaglia et al. (2013) suggested a method for calculating the evolution of the 3-dimensional ionization field in $> (\text{Gpc}/h)^3$ volumes using the correlation between the ionization field and dark matter overdensity field at different redshifts from high resolution radiation-hydrodynamic simulations. This method accurately reproduces the ionization structure on the scales tested but does not show an increase in large scale power when the box size is increased, as has been shown in the direct simulations of Iliev et al. (2013).

In this paper we introduce a new method to perform very large volume ($> \text{Gpc}/h$ box size) reionization simulations, whilst modelling the galaxy formation physics using smaller volumes ($100\text{Mpc}/h$ box size). Our model is based on the GALFORM galaxy formation model (Bower et al. 2006; Lagos et al. 2012). We employ GALFORM within the Millennium-II simulation (Boylan-Kolchin et al. 2009), and combine it with a semi-numerical scheme to calculate the structure of reionization as described in Kim et al. (2013). We begin in §2 by briefly describing the implementation of GALFORM, and our method for simulating reionization. Then, in §3 we describe our method for translating the galaxy formation physics to large volume reionization simulations. We discuss some implications in §4, and finish with our Summary in §5.

2 A SEMI-NUMERICAL MODEL FOR REIONIZATION

In this section we briefly introduce reionization modelling based on the method described in Kim et al. (2013). We combine the semi-analytic galaxy formation model GALFORM (§2.1) with an improved semi-numerical scheme (§2.2) to generate an ionization field. In §2.3 we present the resulting redshifted 21-cm power spectrum.

2.1 The GALFORM galaxy formation model

The GALFORM semi-analytic galaxy formation model successfully explains a large range of observed properties of galaxies at low redshifts (Kim et al. 2011, 2012; Lagos et al. 2012; Kim et al. 2013, 2015). GALFORM includes a range of processes that are thought to be important for galaxy formation (see Cole et al. 2000; Baugh 2006; Bower et al. 2006; Lagos et al. 2012, for more details). In this paper, we implement GALFORM in halo merger trees extracted from the Millennium-II cosmological N-body simulation (Boylan-Kolchin et al. 2009); see Jiang et al. (2014) for a description of the construction of merger trees. The Millennium-II simulation has a cosmology with fractional mass and dark energy densities values of $\Omega_m = 0.25$, $\Omega_b = 0.045$ and $\Omega_\Lambda = 0.75$, a dimensionless Hubble constant of $h=0.73$, and a power spectrum normalisation of $\sigma_8=0.9$ (Millennium cosmology for table 2). The resolution of the simulation is fixed at a halo mass of $\sim 10^8 M_\odot/h$ in the simulation box of side length $L=100\text{Mpc}/h$. Note that we use the Lagos et al. (2012) implementation of GALFORM for this paper.

2.2 Semi-Numerical scheme

We use semi-numerical modelling (e.g. Mesinger & Furlanetto 2007; Geil & Wyithe 2008; Zahn et al. 2007) which is an approximate but efficient method for simulating the reionization process. Because our modelling is based on the Millennium-II simulation, which has positional information for dark matter haloes and galaxies, we begin by gridding the ionizing luminosities of galaxies from the GALFORM model into small volumes (or cells). We assume the number of photons produced by galaxies in the cell that enter the IGM and participate in reionization to be

$$N_{\gamma,\text{cell}} = f_{\text{esc}} \int_0^{t_z} \dot{N}_{\text{Lyc},\text{cell}}(t) dt, \quad (1)$$

where f_{esc} is the escape fraction of ionizing photons produced by stars in a galaxy and t_z is the age of the Universe at redshift z . The total Lyman continuum luminosity of the N_{cell} galaxies within the cell, expressed as the rate of emission of ionizing photons (i.e. units of photons/s), computed from GALFORM is

$$\dot{N}_{\text{Lyc},\text{cell}}(t) = \sum_{i=1}^{N_{\text{cell}}} \dot{N}_{\text{Lyc},i}(t), \quad (2)$$

where

$$\dot{N}_{\text{Lyc},i}(t) = \int_{\nu_{\text{thresh}}}^{\infty} \frac{L_{\nu,i}(t)}{h\nu} d\nu, \quad (3)$$

$L_{\nu,i}$ is the spectral energy distribution of galaxy i , and ν_{thresh} is the Lyman-limit frequency, $h\nu_{\text{thresh}} = 13.6 \text{ eV}$.

We then calculate the ionized hydrogen fraction within each cell according to

$$Q_{\text{cell}} = \left[\frac{N_{\gamma,\text{cell}}}{(1 + F_c)N_{\text{H},\text{cell}}} \right], \quad (4)$$

where F_c denotes the mean number of recombinations per hydrogen atom up to reionization and $N_{\text{H},\text{cell}}$ is the number of hydrogen atoms within a cell. We choose the values f_{esc} and F_c to get a similar evolution of mean global mass averaged ionized hydrogen fraction to the one shown in Lidz et al. (2008) (see detailed values in Kim et al. 2013). We note that our assumption is that values of F_c and f_{esc} do not depend on the galaxy mass or redshift. In reality the escape fraction may be mass and redshift dependent, and the mean number of recombinations per hydrogen atom may be dependent on the overdensity of intergalactic medium (Inoue et al. 2006; Gnedin et al. 2007; Wyithe & Morales 2007; Wise & Cen 2009; Kuhlen & Faucher-Giguère 2012; Yajima et al. 2011; Kim et al. 2013). The latter quantity is calculated as

$$N_{\text{H},\text{cell}} = n_{\text{H}}(\delta_{\text{dm},\text{cell}} + 1)V_{\text{cell}}, \quad (5)$$

where we assume that the overdensity of hydrogen atoms follows the dark matter (computed based on the Millennium-II simulation density field, $1 + \delta_{\text{dm},\text{cell}} = \rho_{\text{dm},\text{cell}}/\bar{\rho}_{\text{dm}}$), n_{H} is the mean comoving number density of hydrogen atoms, and V_{cell} is the comoving volume of the cell. Self-reionization of a cell occurs when $Q_{\text{cell}} > 1$. We divide the Millennium-II simulation box into either 256^3 or 50^3 cells, yielding cell side lengths of $0.3906\text{Mpc}/h$ or $2\text{Mpc}/h$, and comoving volumes of $0.0596\text{Mpc}^3/h^3$ or $8\text{Mpc}^3/h^3$ respectively.

Since Q_{cell} can take a value greater than 1, radiation

Table 1. The values of the expected mean global mass averaged ionized hydrogen fractions, $\langle x_i \rangle$, from the semi-analytic model for different redshifts (selected for comparison with the work by Lidz et al. (2008)) and values of the expected mean global mass averaged neutral hydrogen fractions, $\langle x_{\text{HI}} \rangle$. Results of the values of mean mass averaged neutral hydrogen fraction, $\langle x_{\text{HI,Semi}} \rangle$, from the semi-numerical scheme for different redshifts. This case assumed the default model with Millennium-II and the Lagos et al. (2012) GALFORM model.

Redshift (z)	9.278	8.550	7.883	7.272	6.712	6.197
$\langle x_i \rangle$	0.056	0.16	0.36	0.55	0.75	0.95
$\langle x_{\text{HI}} \rangle$	0.944	0.84	0.64	0.45	0.25	0.05
$\langle x_{\text{HI,Semi}} \rangle$	0.98	0.85	0.67	0.47	0.25	0.059

from a cell with $Q_{\text{cell}} > 1$ can ionize a neighbouring cell with $Q_{\text{cell}} < 1$. In order to find the extent of ionized regions we therefore filter the $N_{\gamma,\text{cell}}$ and $N_{\text{H},\text{cell}}$ fields using a sequence of real-space top hat filters of radius R (from the cell size to box size), producing one smoothed ionization field Q_R per radius calculated by

$$Q_R = \left[\frac{N_{\gamma,R}}{(1 + F_c)N_{\text{H},R}} \right], \quad (6)$$

where $N_{\gamma,R}$ ($N_{\text{H},R}$) is the sum of the number of photons (sum of number of hydrogen atoms) in a sphere of radius R . At each point in the simulation box, we find the largest R for which the filtered ionization field is greater than unity (i.e. ionized with $Q_R > 1$). All cells within radius R around this point are considered ionized. We also include partial ionization for cells (from Eq. 4).

Our method treats each cell as a source. To find HII regions which properly conserve photons from sources when the HII regions overlap, we take the following steps (Zahn et al. 2007; Thomas et al. 2009). We use real space spherical filtering, and so have information regarding which HII bubbles overlap (this is not possible in Fourier space). When filtering we start with the smallest radius corresponding to the size of cell and increase to the size of simulation box (increasing the filtering radius in linear intervals). To properly include overlap between HII regions in the semi-numerical scheme⁴, we consider two cases (shown schematically in Fig. 1). We refer to the cell at the centre of region i with radius R_i as the main cell.

Case 1 : Cells i & j separated by distance D have bubble radii such that bubble j is enclosed within bubble i ($R_i > R_j$). In this case we add all photons when calculating Q_{R_i} .

Case 2: The separation D between two cells is smaller than the sum of their two bubble radii. This case corresponds to the partial overlap of neighbouring HII bubbles. To conserve the number of photons from cells in this case,

⁴ Note that Kim et al. (2013) used real space top hat filters of radius from the box size to the cell size. The filtering from large radius to small radius resulted in double counted photons in the overlap regions of neighbouring bubbles, and so the model did not satisfy photon conservation. Our calculations in this paper improve photon conservation relative to the method in Kim et al. (2013).

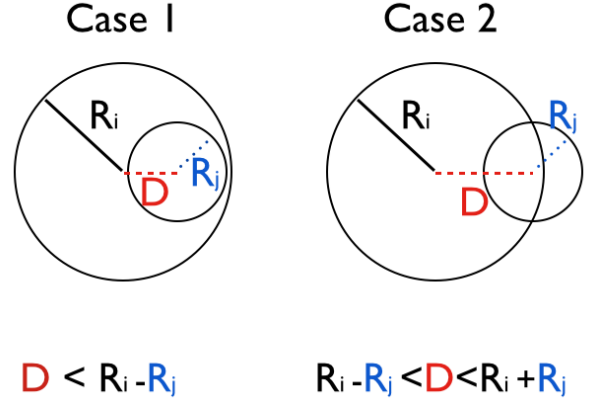


Figure 1. The different two cases of overlap between two HII bubbles. R_i and R_j are the radii of two individual bubbles and D is the distance between the centres of the bubbles i and j .

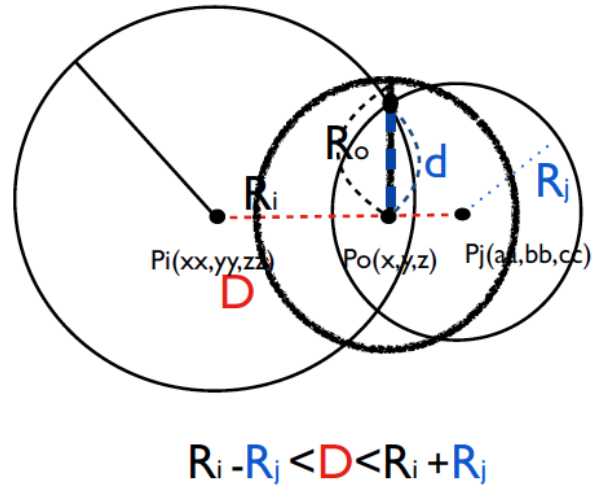


Figure 2. The semi-numerical scheme to include overlap between two HII bubbles. R_i and R_j are the radii of two individual bubbles and D is the distance between the centres of the bubbles i and j . The third HII bubble (radius R_o) is centred at a point of internal division (P_o) between the two HII bubbles in the overlap area.

we follow previous work which noted that photons inside the region of overlap between two HII bubbles may not increase the individual sizes of the two HII individual bubbles (Zahn et al. 2007; Thomas et al. 2009). Instead, these photons are likely to ionize an additional volume near the intersection between the two HII bubbles. To model this overlap, we have used a semi-numerical scheme to initially find the two HII regions. Based on the positions and radii of these HII bubbles, we add a third bubble centred at P_o and of radius R_o (see Fig. 2). P_o is defined to be the centre of the circle of intersection of the two bubbles, and we define $R_o = F_{\text{overlap}} \times d$, where d is the radius of this circle. F_{overlap} is a free parameter, and we use $F_{\text{overlap}} = 1.2$, which results in approximate photon conservation across the redshift range. We ionize all cells within the third bubble. To treat the case of more than 2 overlapping bubbles, we span all possible overlapping regions between all sources. We check for double counting of photons during this process by neglecting already accounted for ionizing sources.

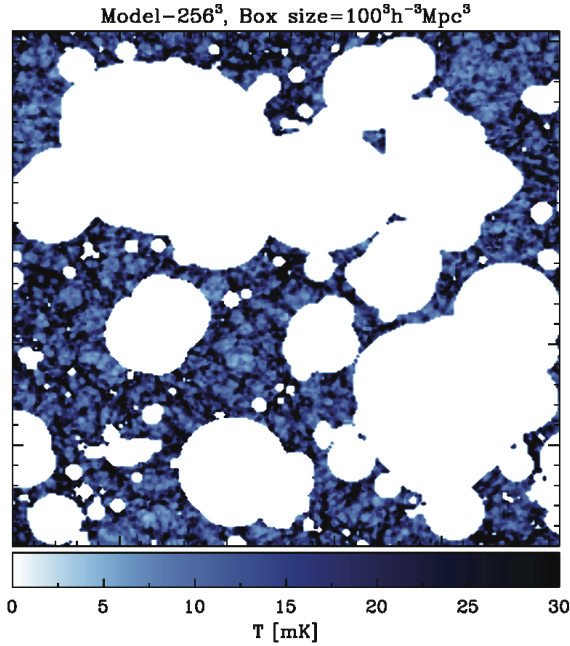


Figure 3. The 21cm intensity map from the Model-256³ (cell size 0.39Mpc/h) at $z \sim 7.272$ ($\langle x_i \rangle \sim 0.55$) with slice that is 0.39Mpc/h deep. The colour shading shows the 21cm intensity in temperature units, as indicated by the bar.

Based on our assumption for escape fraction and F_c , we calculate the expected mean global mass averaged ionized hydrogen fraction from the ratio between ionizing photons and hydrogen atoms. $\langle x_i \rangle = N_{\gamma, \text{tot}} / [(1 + F_c) N_{\text{H, tot}}]$, where $N_{\gamma, \text{tot}}$ ($N_{\text{H, tot}}$) is the sum of the number of photons (sum of the number of hydrogen atoms) in the simulation. The expected mean global mass averaged neutral hydrogen fraction is then obtained from the relation $\langle x_{\text{HI}} \rangle = 1 - \langle x_i \rangle$. We also calculate the neutral hydrogen fraction resulting from the semi-numerical scheme by averaging over the ionization state in the simulation volume ($\langle x_{\text{HI, Semi}} \rangle$). If the model is working correctly, $\langle x_{\text{HI}} \rangle = \langle x_{\text{HI, Semi}} \rangle$, and the semi-numerical scheme perfectly conserves photons.

An example calculation of the ionization structure from the Millennium-II simulation and GALFORM model (Lagos et al. 2012) is shown in Fig. 3. To illustrate the conservation of ionizing photons in our model, Table 1 shows the mean mass averaged neutral hydrogen fractions, $\langle x_{\text{HI, Semi}} \rangle$, from the semi-numerical output, together with the expected mean global mass averaged ionized (neutral) hydrogen fraction, $\langle x_i \rangle$ ($\langle x_{\text{HI}} \rangle$) from the semi-analytic model for different redshifts. The mean mass averaged neutral hydrogen fractions using the semi-numerical scheme agree well with the values of $\langle x_{\text{HI}} \rangle$, with less than 5 percent variance across the range of redshifts.

2.3 Redshifted 21-cm intensity and power spectrum

We next consider predictions for the 21cm power spectrum. In this paper we restrict our attention to analyses that assume the spin temperature of hydrogen is coupled to the

kinetic temperature of an IGM that has been heated well above the CMB temperature ($z \lesssim 9$ & $T_s \gg T_{\text{CMB}}$, see Santos et al. 2008). This restriction is a limitation of the semi-numerical model in Kim et al. (2013). However we note that the method described in this paper to extend the statistics in a small simulation to larger volumes could incorporate more sophisticated models. In this regime, ignoring the contribution to the amplitude from velocity gradients and assuming the hydrogen overdensity follows the dark matter ($1 + \delta_{\text{dm, cell}}$), there is a proportionality between the ionized hydrogen fraction and 21 cm intensity. The 21 cm brightness temperature contrast may therefore be written as

$$\Delta T(z) = T_0(z) [1 - Q_{\text{cell}}] (1 + \delta_{\text{dm, cell}}), \quad (7)$$

where $T_0(z) = 23.8 \sqrt{(1+z)/10}$ mK. The filtering procedure described above provides 3-dimensional maps of the ionization structure, and therefore allows us to calculate the 21-cm intensity within the simulation volume. From this we calculate the dimensionless 21-cm power spectrum

$$\Delta^2(k) = k^3 / (2\pi^2) P_{21}(k, z) / T_0(z)^2 \quad (8)$$

as a function of spatial frequency k , where $P_{21}(k)$ is the 3-dimensional power spectrum of 21-cm brightness temperature $\Delta T(z)$ (described by eq. (7)).

The predicted power spectrum for the default model is shown as the solid curve in the top (bottom) right panel of Fig. 4 at $z=7.272$ (7.883)⁵. We include a statistical error on the power spectrum calculated as the uncertainty $\sigma(k) = \sqrt{\frac{2}{n_{\text{modes}}}} \times \Delta^2(k)$, where the n_{modes} is the number of Fourier modes present in a spherical shell of width δk within volume of V . For large scales, $k \ll 2\pi/V^{1/3}$, $n_{\text{modes}} = V 4\pi k^2 \delta k / (2\pi)^3$, where $\delta k = 2\pi/V^{1/3}$.

3 REIONIZATION IN A LARGE VOLUME SIMULATION.

In the previous section, we introduced a semi-numerical model for reionization based on GALFORM and the Millennium-II simulation. Although simulations continue to increase in size, the method is therefore limited to volumes in which halo masses can be included down to the lowest masses thought to be responsible for reionization.

However, larger volume reionization simulations are needed both to make mock observations for understanding forthcoming observations of the epoch of reionization (EoR), and also to correctly describe the amplitude of the redshifted 21cm power spectra at large scales.

Iliev et al. (2013) used radiative transfer to study reionization within a very large volume simulation. Iliev et al. (2013) show that the large scale power spectrum does not converge unless box sizes as large as 425Mpc/h are used. Because such large volume simulations are very expensive, a method to use large volume intermediate resolution simulations from smaller volume high resolution simulations was introduced by Battaglia et al. (2013). Battaglia et al. (2013)

⁵ Note that we plot the power spectrum for wavenumbers less than $\sim 0.6 k_N$ where k_N is the Nyquist frequency of the grid to avoid the features introduced by mass assignment in a grid (cf. Cui et al. (2008)).

extract the correlation between the ionization field and dark matter overdensity field as a function of redshift using a high resolution radiation-hydrodynamic simulation. They then construct a parametric function for the bias which is used to filter a large scale density field to derive the corresponding large scale spatially varying reionization-redshift field. This method to produce large volume reionization simulations is fast. However, the results in Battaglia et al. (2013) do not show the difference between large volume and small volume calculations of the 21cm power spectrum amplitude at large scales that is seen in the simulations of Iliev et al. (2013).

Therefore, we suggest a method to simulate a large volume to study reionization which has a sophisticated galaxy formation model to follow ionizing sources, is reasonably fast, and correctly calculates the amplitude of the power spectrum on large scales. To describe the contribution of small galaxies during the EoR, we need a dark matter simulation which can resolve sources in $\sim 10^8 M_\odot/h$ halos which are thought to dominate the production of ionizing photons (Iliev et al. 2007). For this reason we have combined the GALFORM semi-analytic galaxy formation model with our semi-numerical scheme to simulate HII region growth within the Millennium-II simulation box of 100Mpc/h size (Kim et al. 2013). As can be seen in Fig. 3, a box of 100Mpc/h size may not be large enough as ionized features can fill a significant fraction of the simulation volume, even at a mean mass averaged neutral hydrogen fraction of 0.45.

In this section we describe a method to predict the 21-cm intensity map during reionization within larger volumes. The simulations we use for this include the Millennium (Springel et al. 2005), the GigggleZ (Poole et al. 2014) and the Millennium-XXL (MXXL, Angulo et al. 2012) simulations. These large volumes are required to model forthcoming 21cm simulations. Note that we rescale the dark matter density distributions of the Millennium, MXXL and GigggleZ-main simulations to match the Millennium-II simulation in order to avoid different results caused by different redshift outputs (between $z=7.272$ and $z=7.33$) or different cosmologies. This rescaling is necessary because different output redshifts or different cosmologies lead a deviation in the distribution width of dark matter overdensities. We adjust for this deviation by adding a multiplicative factor to the logarithm of each density contrast (e.g., $\sim 1.1 \times \log(1+\delta_{\text{dm,GigggleZ}}) = \log(1+\delta_{\text{dm,Millennium-II}})$). A summary of dark matter simulations is given in Table 2.

3.1 Monte Carlo realization of the Q_{cell} values within dark matter simulations

Before discussing application to large volumes we develop our method within the Millennium-II simulation, allowing us to test for systematics and errors in the method. We extract the Q_{cell} distribution of values (from eq. 4) as a function of dark matter overdensity (from the Millennium II dark matter simulation) using the luminosities from the GALFORM galaxy formation model. We refer to this default model as the Model-256³ and to this distribution as the **Qvalue Dark matter overdensity Occupation Distribution; QDOD**. The top (bottom)-left panel of Fig. 4 shows the distribution of Q_{cell} values as a function of dark matter overdensity for all pixels in the Model-256³ model at $z=7.272$ (7.883).

The physics of galaxy formation produces a complex,

nonlinear relation between the dark matter overdensity and Q_{cell} values. To populate the distribution of Q_{cell} values as a function of dark matter overdensity, we have binned by dark matter overdensity and measured the probability distribution of Q_{cell} values in each overdensity bin, $P[Q_{\text{cell}}|(1+\delta_{\text{dm,cell}})]$. To calculate the reionization structure within a large volume from the relation between the dark matter overdensity and Q_{cell} values, we then use a Monte-Carlo technique to populate the dark matter simulation (smoothed on the spatial scale of the cells in the reionization simulation) with Q_{cell} values from this distribution.⁶ We calculate the $N_{\gamma,\text{cell}}$ and $N_{\text{H,cell}}$ using eqs. 4 and 5 based on the populated Q_{cell} values and $\delta_{\text{dm,cell}}$ in a large volume simulation. We follow the semi-numerical scheme as described in §2.2 to find the ionization structure. In order to find the extent of ionized regions we therefore filter the resulting $N_{\gamma,\text{cell}}$ and $N_{\text{H,cell}}$ fields using a sequence of real-space top hat filters of radius R (from the cell size to box size), producing one smoothed ionization field Q_R per radius using eq. 6. We find the largest R for which the smoothed ionization field is greater than unity (i.e. ionized with $Q_R > 1$). All cells within radius R around this point are considered ionized. We then account the overlap region of adjacent HII bubbles as in §2.2 to achieve photon conservation.

We note that this approach does not capture the possible correlation of ionization luminosities for cells separated by a distance r , and so may introduce noise into the ionization map due to the random assignment of ionizations at fixed $\delta_{\text{dm,cell}}$. However, we show that the effect of this on the power spectrum is negligible over large volumes, although the ionization field does show small differences on small scales (see the GigggleZ-500³ models in Fig. 11). Moreover, on large scales the method does capture the very large scale clustering of ionising radiation in the linear regime, because the clustering of overdensities is described by the large volume N-body simulation.

To test our method, we show the resulting ionization maps in Fig. 5 from two Monte-Carlo models calculated within the Millennium-II dark matter simulation (hereafter MC-256³-I and II) on which the default Model-256³ was based. We also show the corresponding 21cm power spectrum in the top and bottom right panels of Fig. 4 for $z=7.272$ and 7.883. The right panels of Fig. 4 show that the amplitudes and overall shapes of the 21cm power spectra from the MC-256³ realisations are in reasonable agreement with Model-256³. However, the amplitudes of 21cm power spectra from MC-256³ models are $\sim 10\%$ lower than the Model-256³ at large scales for both redshifts (see the ratio of MC-256³ models to the Model-256³ in bottom sub-panels of right panels of Fig. 4).

⁶ For comparison, Battaglia et al. (2013) reconstruct the ionization field using the best fit parametric form obtained from the radiation-hydrodynamic high resolution simulation that describes the correlation between the reionization redshift and dark matter overdensity field as a function of redshift.

Table 2. Some basic properties of the dark matter simulations used in the paper. L_{box} is the side length of the simulation box, N_p is the total number of simulation particles used, and ϵ is the Plummer-equivalent force softening of the simulation, in comoving units. m_p gives the mass of each simulation particle.

	L_{box} [Mpc/h]	N_p	ϵ [kpc/h]	m_p [M_\odot/h]	cosmology
Millennium-II	100	10,077,696,000	1.0	6.89×10^6	Millennium
Millennium	500	10,077,696,000	5.0	8.61×10^8	Millennium
Millennium-XXL	3000	303,464,448,000	10.0	6.17×10^9	Millennium
GiggleZ-main	1000	10,077,696,000	9.3	7.52×10^9	WMAP5

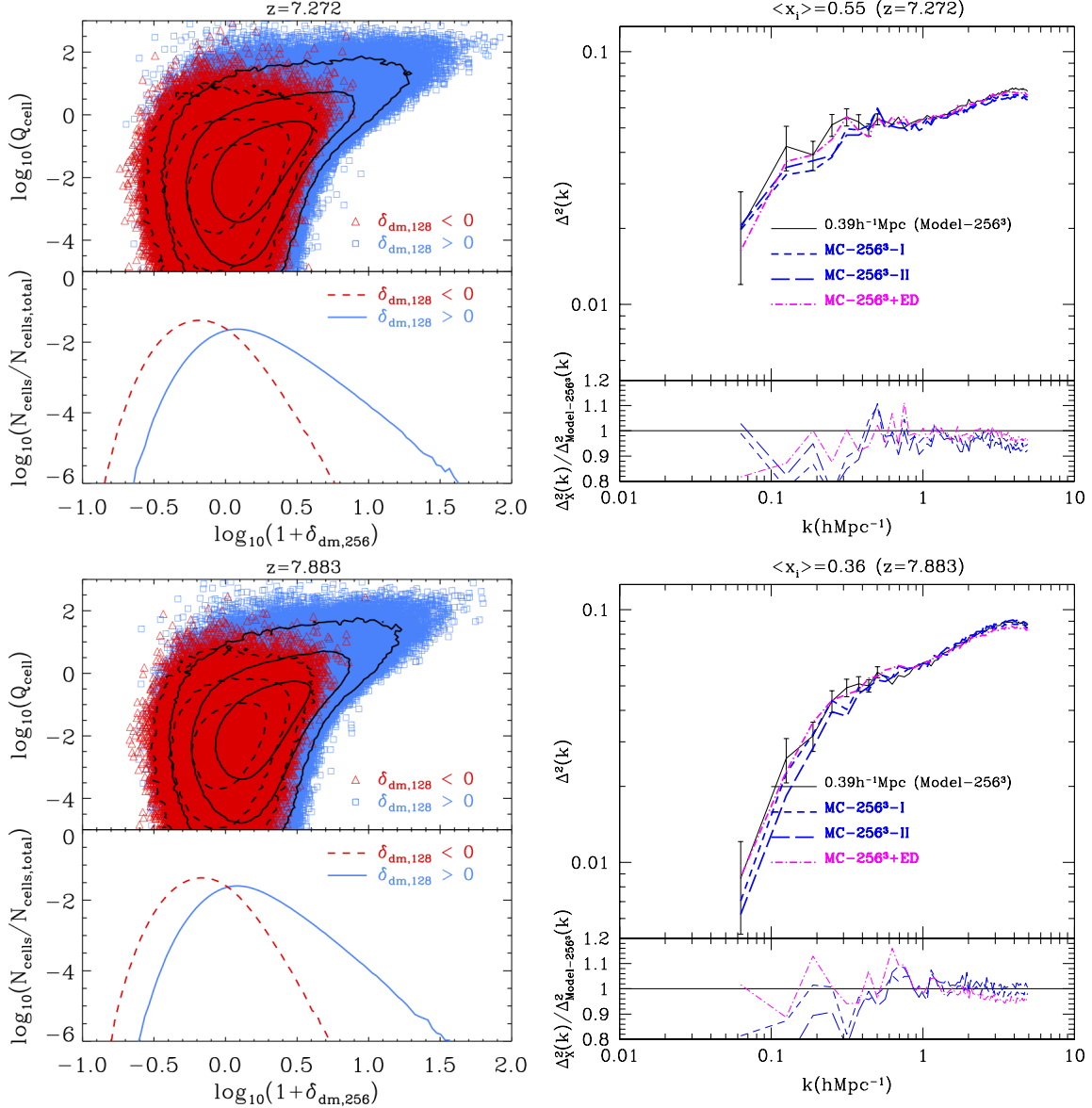


Figure 4. Left panels show the distribution of Q values (top sub-panels) as a function of dark matter overdensity and number distributions of dark matter overdensities (bottom sub-panels) in the Model-256³ simulation at two redshifts ($z=7.272$ (top), 7.883 (bottom)). The blue squares and red triangles correspond to over and under dense regions on large scale. The solid (dashed) line contours in left panels show 68.3%, 95.4%, and 99.7% of this distribution for over (under) dense region. Right panels show the 21-cm power spectrum predictions using the Model-256³, MC-256³ models (blue lines) and MC-256³+ED model (magenta line) for two redshifts. The fractional difference relative to the 256³ model power spectrum is shown in the lower sub panel.

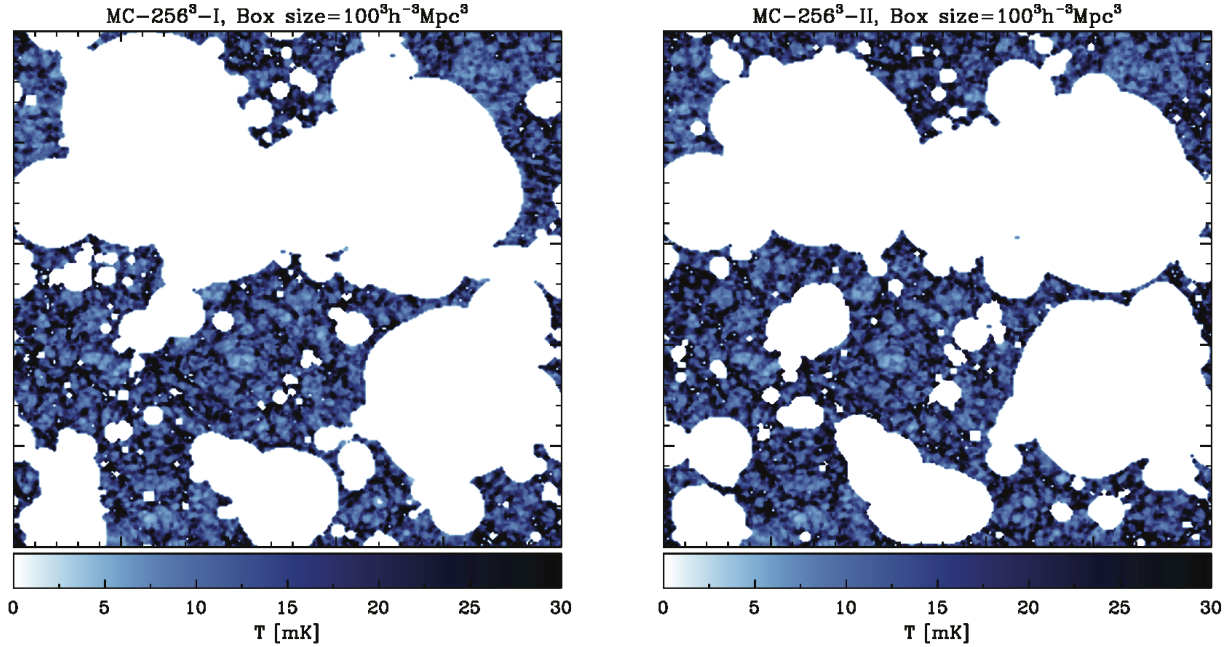


Figure 5. Realisations of 21cm intensity maps of the MC-256³ (cell size 0.39Mpc/h) models at $z \sim 7.272$ ($\langle x_i \rangle \sim 0.55$) with slices that are 0.39Mpc/h deep. The colour shading shows the 21cm intensity in temperature units, as indicated by the bar.

3.2 Environmental dependence on Q_{cell}

To improve the calculation, we note that Q_{cell} is related to not only dark matter overdensity but also the environment of dark matter overdensity. We therefore choose a larger cell ($\sim \times 8$ in volume) surrounding the point containing the value of Q_{cell} to include any environmental effects. We summarise the cell size of models and the environmental cell size of models including the environmental effect in Table 3. The left panels of Fig. 4 show the distribution of Q_{cell} values (top-sub panels) in regions of over (blue squares)- and under (red triangles) density within a 128^3 grid ($\delta_{\text{dm},128}$) at $z=7.272$ and $z=7.883$. The solid (dashed) line contours in the sub panels of Fig. 4 enclose 68.3%, 95.4%, and 99.7% of this distribution for over (under) dense regions, respectively. Q_{cell} values on the 256^3 grids in the high overdensity group have statistically larger values than those in the low overdensity group. We incorporated both conditional probabilities for Q_{cell} ($P[Q_{\text{cell}}|(1+\delta_{\text{dm},256})](\delta_{\text{dm},128} > 0)$ and $P[Q_{\text{cell}}|(1+\delta_{\text{dm},256})](\delta_{\text{dm},128} < 0)$) into our realisations. The realisation including this large scale environmental dependence better matches the amplitude of the model 21cm power spectrum at scales between $k \sim 0.1h/\text{Mpc}$ and $k \sim 0.5h/\text{Mpc}$ (MC-256³+ED in the right panels of Fig. 4). It is therefore important to include the environmental effect in the simulation. We include this large scale environment effect in all subsequent models for the paper.

3.3 Dependence of cell size

Having tested the method, we next expand our calculations to larger volumes. In order to do this it is convenient to increase the cell size. We have therefore smoothed the cell size of our default simulation within the Millennium-II to

2Mpc/h rather than the 0.39 Mpc/h used in Fig. 4. As a result we decrease the number of cells in the Millennium-II simulation from 256^3 to 50^3 cells. We refer to this as the Model-50³ simulation.

Fig. 6 shows results for this lower resolution that correspond to those in Fig. 4 for the Q_{cell} value distribution as a function of overdensity (with environment effect; i.e., red triangles and blue squares). We see that the Q_{cell} value distribution from the Model-50³ model has a much tighter relation than in the Model-256³ model both $z=7.272$ and 7.883 , as a result of smoothing on the larger grid. The solid (dashed) line contours in the left panels of Fig. 6 show 68.3%, 95.4%, and 99.7% of this distribution for over (under) dense regions, respectively. We use this QDOD as described in §3.1 to calculate Monte-Carlo realizations of the ionization structure on a 50^3 grid. Two examples are shown in Fig. 7. The corresponding redshifted 21-cm power spectra from these two models are noisy, but again show good agreement (see Fig. 6). For comparison, we also show the power spectrum from the Model-256³. Importantly the agreement between the Model-50³ and the Model-256³ power spectra is good. These calculations provide a demonstration that our method for constructing Monte-Carlo ionization fields within the parent volume of the reionization simulation produces accurate power spectra, and is insensitive to the grid resolution.

3.4 Application to larger volumes

We next apply our method for generating 21-cm intensity maps to the Millennium and the GigglyZ-main simulations. As above, we generate Q_{cell} values in the Model-50³ model which is based on the Millennium II dark matter simulation

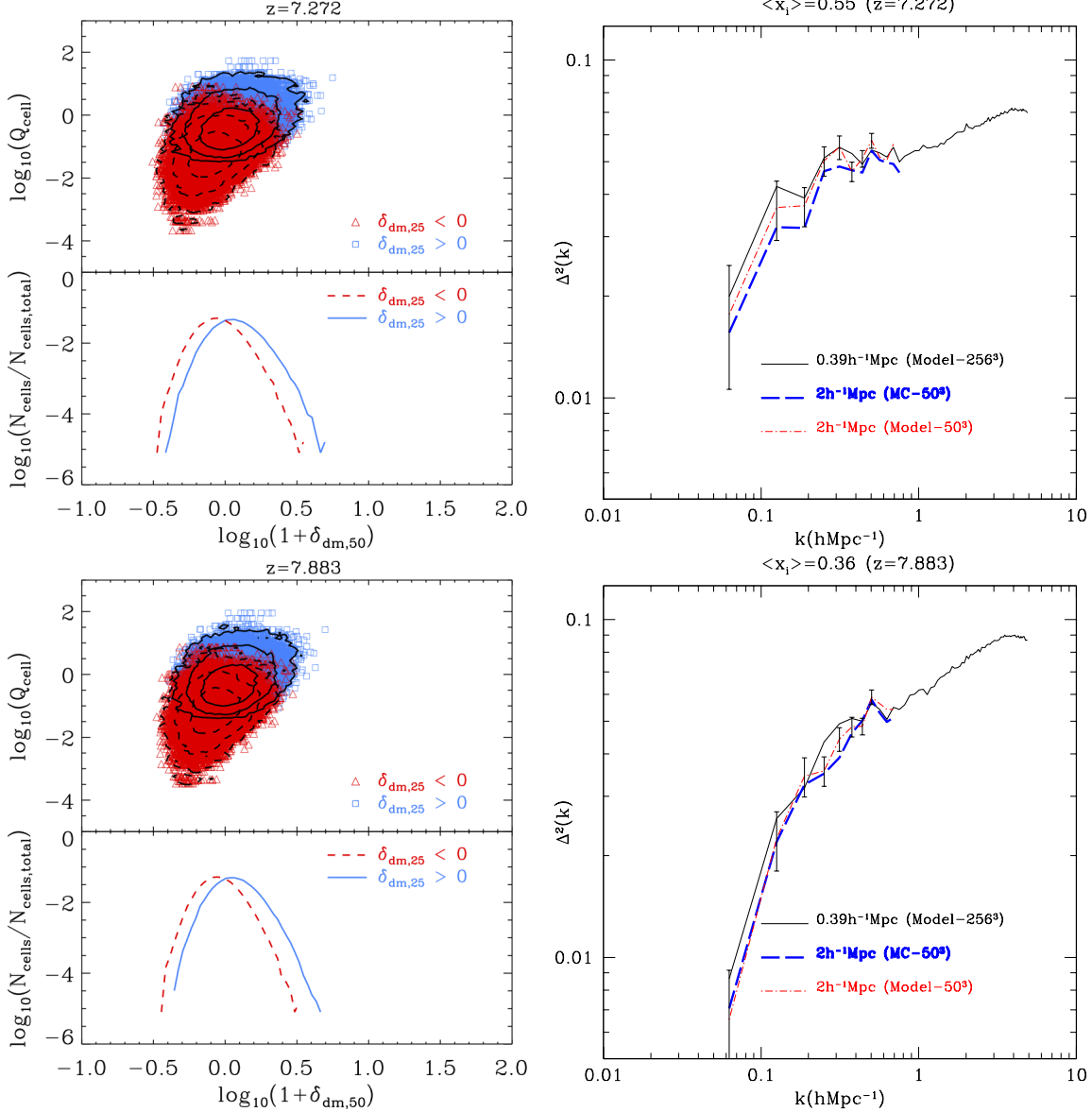


Figure 6. Left panels show the distribution of Q value (top sub-panels) as a function of dark matter overdensity and number distributions of dark matter overdensities (bottom sub-panels) in the Model-50³ simulation a 2Mpc/ h cell size at $z=7.272$ and 7.883. The blue squares and red triangles correspond to over and under dense regions. The solid (dashed) line contours in left panels show 68.3%, 95.4%, and 99.7% of this distribution for over (under) dense region on large scale. Right panels show the 21-cm power spectrum predictions by the Model-50³ and MC-50³ simulations with the Model-256³ simulation for comparison at two redshifts.

and includes the low mass galaxies that drive reionization. The Model-50³ model has a cell size of 2Mpc/ h . This cell size corresponds to a grid size of 250³ cells in the Millennium simulation and 500³ cells in the GiggleZ-main simulation (cf. see also Ahn et al. (2012) for sub-grid modelling). A summary of models is given in Table 3.

Fig. 8 shows the resulting reionization maps. The corresponding 21-cm power spectra for these models are shown in Fig. 11. The 21-cm power spectra from the models show good agreement for wavenumbers k between 0.1 h /Mpc and 1 h /Mpc. However the larger 21-cm maps, from the Millennium and GiggleZ-main simulations, allow the 21-cm power spectrum to be extended to much larger scales. We also include a model that does not include supernovae feed-

back (hereafter GiggleZ-500³-NOSN) based on the NOSN-0 model in Kim et al. (2013). For the NOSN model, we turn off feedback by supernovae in the default model, and change the free parameters (f_{esc} and F_c) to obtain $\langle x_i \rangle = 0.55$. The 21-cm map in the left panel of Fig. 9 shows that the typical HII bubble size is much smaller than for models which include supernovae feedback. This is imprinted on the 21-cm power spectrum in Fig. 11 which shows that the amplitude of the 21-cm power spectrum for the GiggleZ-500³-NOSN model is much lower than the default model. This is because the NOSN model has a much larger contribution to the ionizing photon budget from low mass haloes than the default model (see more details in Kim et al. 2013).

To further test whether the Monte-Carlo method in-

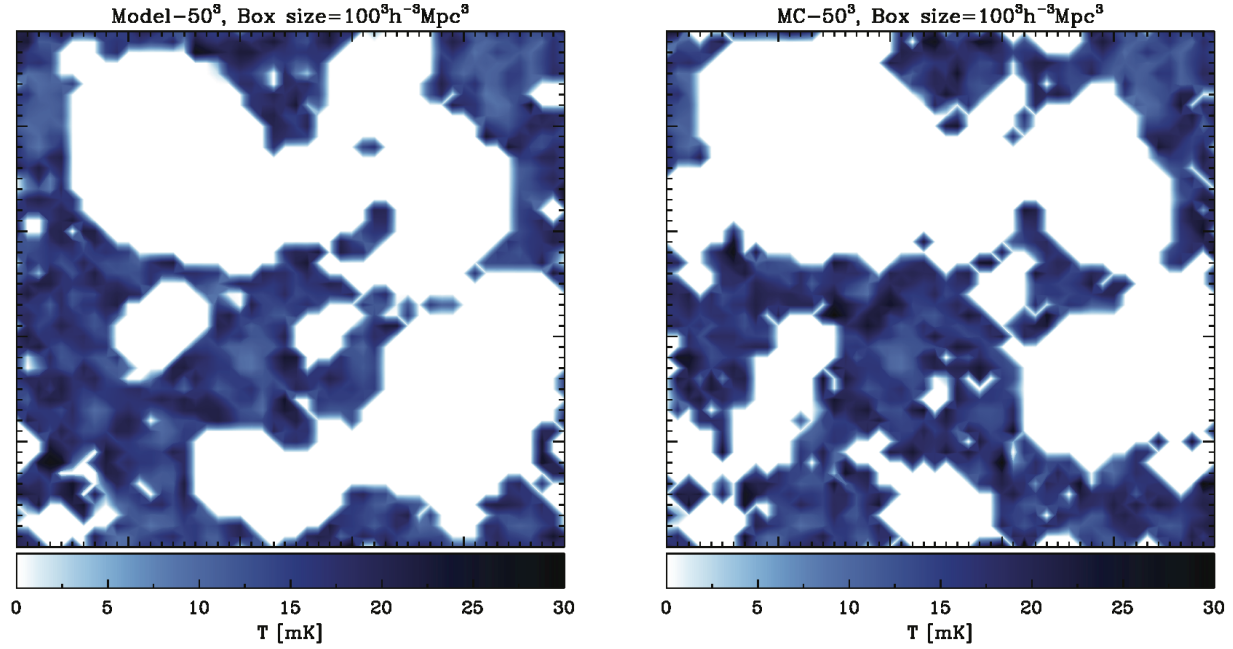


Figure 7. The 21cm intensity maps of the Model-50³ and the MC-50³ models at $z \sim 7.272$ ($\langle x_i \rangle \sim 0.55$) with cell size 2Mpc/h in Sec. 3.3 and 2Mpc/h deep. The colour shading shows the 21cm intensity in temperature units, as indicated by the bar.

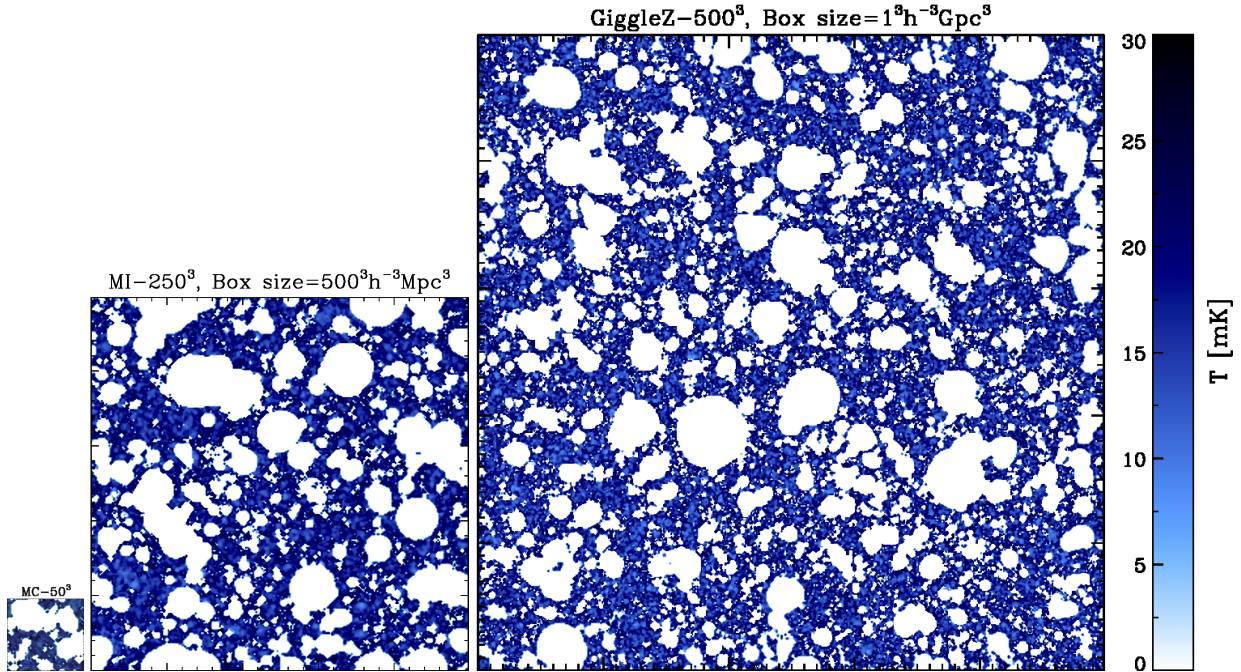


Figure 8. The three panels show the 21-cm intensity maps from the MC-50³ (100Mpc/h box size), MI-250³ (500Mpc/h), and GiggleZ-500³ (1000Mpc/h) models at $z \sim 7.272$ ($\langle x_i \rangle \sim 0.55$) with cell size 2Mpc/h. All models use the Lagos11 model. The size of the figures correspond to the relative box size of simulations. The slices are 2Mpc/h deep.

introduces power into the intensity distribution, we have generated another random realisation within the GiggleZ-main simulation (hereafter the GiggleZ-500³-I model). If the QDOD works correctly these two realisations should be statistically similar. The right panel of Fig. 9 shows the result-

ing 21-cm map, with the corresponding 21-cm power spectra plotted in Fig. 11. Small scale differences can be seen by comparing the intensity maps for the GiggleZ-500³ and GiggleZ-500³-I. However, the power spectra are the same at the percent level across the full range of wavenumber k , in-

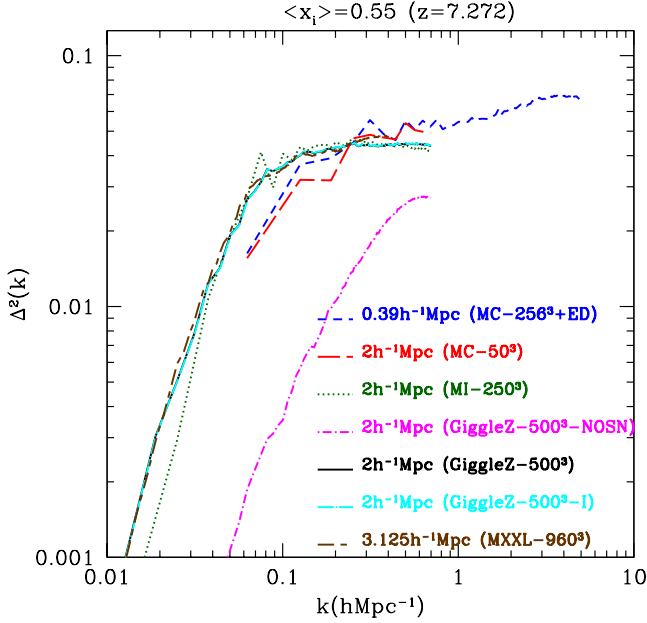


Figure 11. 21cm power spectrum predictions with comparison to the power spectrum from the high resolution simulation MC-256³ model. The simulations are labelled in the figure.

dicating that the small differences seen in the power spectra shown in Fig. 4 were due to the small volume rather than being due to stochasticity in the method.

We next apply the QDOD method to the Millennium XXL simulation which has a 3Gpc/h box size (hereafter MXXL-960³ model). We use the QDOD from the Model-256³ model smoothed on a 3.125Mpc/h (32³ grids) to populate Q_{cell} values onto the Millennium XXL dark matter simulation (Fig. 10). The simulated 21-cm power spectrum of these simulations is shown in the Fig. 11. We note that on large scales light-cone effects become important (Battaglia et al. 2013).

4 21CM POWER SPECTRUM PREDICTIONS FROM LARGE VOLUME SIMULATIONS

In this section, we use our simulations to discuss the effect of simulation volumes on the large scale power spectrum (§4.1). We also discuss the large scale 21cm power spectrum predictions from different star formation laws, and the presence of SNe feedback and photoionisation feedback (§4.2).

4.1 Large scale predictions of 21cm power spectrum

Here we investigate predictions for the 21cm power spectrum on the largest scales. Iliev et al. (2013) performed the largest numerical simulations of reionization to date, showing that large scale power continues to increase as volume increases, owing to the effect of large scale power on structure formation. We have used two sets of simulations, binned on a $\sim 2\text{Mpc}/h$ (3.125Mpc/h for the MXXL-960³) scale, to investigate the effect of simulation volume on predictions

for the 21cm power spectrum. One set includes the MC-50³ model (100Mpc/h), the MI-250³ model (500Mpc/h), and the MXXL-960³ model (3Gpc/h) which are based on the Millennium simulation cosmology. The other set is the HR-60³ model (a GiggleZ simulation which has 125Mpc/h box size; hereafter GiggleZ-HR) and the GiggleZ-500³ model (1000Mpc/h). The GiggleZ simulations are based on the WMAP7 cosmology.

The left hand panel of Fig. 12 shows the distribution of dark matter overdensity for these models. The models show nearly identical distributions (note that the MXXL-960³ has a narrower distribution than the other simulations because it is based on a 3.125Mpc/h cell size). However, the relatively small box simulations (MC-50³ and HR-60³ models) have no overdensities greater than 4.5. The right hand panel shows the resulting 21cm power spectra. We see that there is significant extra power in the observational window for $k < 0.1\text{h}/\text{Mpc}$ within the (500Mpc/h)³ volumes of the Millennium, GiggleZ, and MXXL than in the smaller (100Mpc/h)³ simulation. We find that the power spectra have converged at $0.01 \leq k \leq 0.1\text{h}/\text{Mpc}$ for volumes of (500Mpc/h)³. However since larger bubbles form in the highly ionized stage of reionization, we may need even larger volume simulations to see the convergence of the predicted 21cm power spectrum at lower z .

We note that the highest overdensity bins in MI-250³, MXXL-960³, and GiggleZ-500³ models exceed values available in the input MC-50³ model. However, these overdensities are very rare. To test the importance of these large overdensities we put either $Q_{\text{cell}}=0$ or Q_{cell} equal to the highest overdensity bin of MC-50³. The predicted 21cm power spectra from these two different assumptions are nearly identical, indicating that these very rare and large overdensities do not contribute to the statistics of reionization.

4.2 Observational implications

The first-generation low-frequency telescopes, such as MWA and LOFAR, aim to detect the slope and amplitude of the redshifted 21cm power spectrum (Lidz et al. 2008). Following the analysis in Kim et al. (2013) we calculate the slope and amplitude of the predicted redshifted 21cm power spectrum using large volume simulations of reionization. The simulations have a large enough volume to avoid the issue of sample variance near the central wavenumbers ($k=0.2$ and $0.4\text{h}/\text{Mpc}$ corresponding to the point on the power spectrum at which observables will likely evaluate the amplitude and gradient from the MWA). To quantify the effects of star formation law, we use implementations of GALFORM from Lagos et al. (2012) & Bower et al. (2006) (Lagos11 .vs. Bow06)⁷. To quantify the effect of photoionisation feedback, we compare the NOSN($V_{\text{cut}}=30\text{km/s}$) (turn off the SNe feedback) .vs. NOSN (no suppression) (turn off both the SNe and the photoionisation feedbacks) models. We use models with and without photoionisation feedback

⁷ Lagos11 extended GALFORM by modelling the splitting of cold gas in the ISM into its HI and H2 components and by linking star formation explicitly to the amount of H2 present in a galaxy.

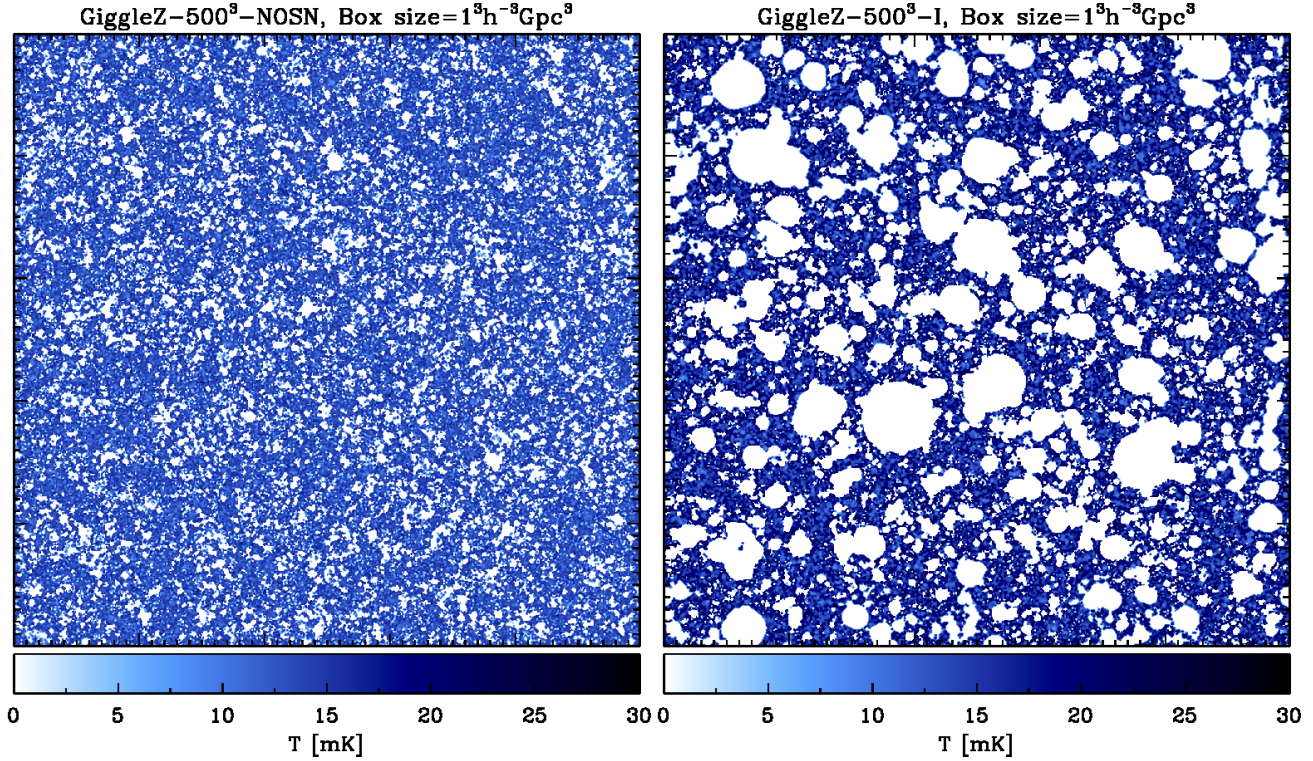


Figure 9. The 21-cm intensity maps for the GiggleZ-500³-NOSN (which use the NOSN galaxy formation model from Kim et al. (2013)) and GiggleZ-500³-I (use the Lagos11 galaxy formation model) simulations at $z \sim 7.272$ ($\langle x_i \rangle \sim 0.55$) with cell size 2Mpc/h. The slices are 2Mpc/h deep.

Table 3. The box size for N-body dark matter simulation we used models in this paper, the number of cells (number of cells to include environmental effect), and cell size (cell size to include environmental effect).

Model	Box size	N-body simulation	# of cells	Cell size
MC-50 ³	100Mpc/h	Millennium-II	50 ³ (25 ³)	2 (4) Mpc/h
MI-250 ³	500Mpc/h	Millennium	250 ³ (125 ³)	2 (4) Mpc/h
HR-60 ³	125Mpc/h	GiggleZ-HR	60 ³ (32 ³)	2.08 (4.16) Mpc/h
GiggleZ-500 ³	1000Mpc/h	GiggleZ-main	500 ³ (250 ³)	2 (4) Mpc/h
GiggleZ-500 ³ -I	1000Mpc/h	GiggleZ-main	500 ³ (250 ³)	2 (4) Mpc/h
GiggleZ-500 ³ -NOSN	1000Mpc/h	GiggleZ-main	500 ³ (250 ³)	2 (4) Mpc/h
MXXL-960 ³	3000Mpc/h	Millennium-XXL	960 ³ (750 ³)	3.125 (4) Mpc/h

(NOSN($V_{\text{cut}}=30\text{km/s}$) .vs. NOSN (no suppression))⁸. Finally to quantify the effect of SNe feedback we compare the model from Bower et al. (2006), with a modified model

in the absence of SNe feedback (NOSN($V_{\text{cut}}=30\text{km/s}$))⁹. Simply removing the feedback strength of SNe results in a model which greatly overpredicts the number of galaxies at all luminosities. In order to approximately reproduce the

⁸ Photoionisation is predicted to have a dramatic impact on star formation in low mass galaxies. In the standard implementation of GALFORM, the effect of photoionisation feedback induced by the epoch of reionization is modelled by imposing a circular velocity cut off $V_{\text{cut}}=30\text{km/s}$ on gas cooling at redshifts below the redshift corresponding to the end of reionization $z_{\text{cut}}=10$. We turn off the photoionization feedback by setting $V_{\text{cut}}=0$ (no suppression of gas cooling).

⁹ The default GALFORM model (e.g., Bow06 and Lagos11) parameterizes the SNe feedback mass loading efficiency as $\beta = (V_{\text{circ}}/V_{\text{hot}})^{-\alpha_{\text{hot}}}$, where V_{circ} is the circular velocity of the galaxy at the half-mass radius. The parameters V_{hot} and α_{hot} are adjustable and control the strength of SNe feedback. The default model has $V_{\text{hot}} = 485\text{km s}^{-1}$ and $\alpha_{\text{hot}}=3.2$ (cf. Bower et al. 2006). We removed the feedback strength of SNe by setting $V_{\text{hot}}=0$ whilst keeping the photoionisation feedback.

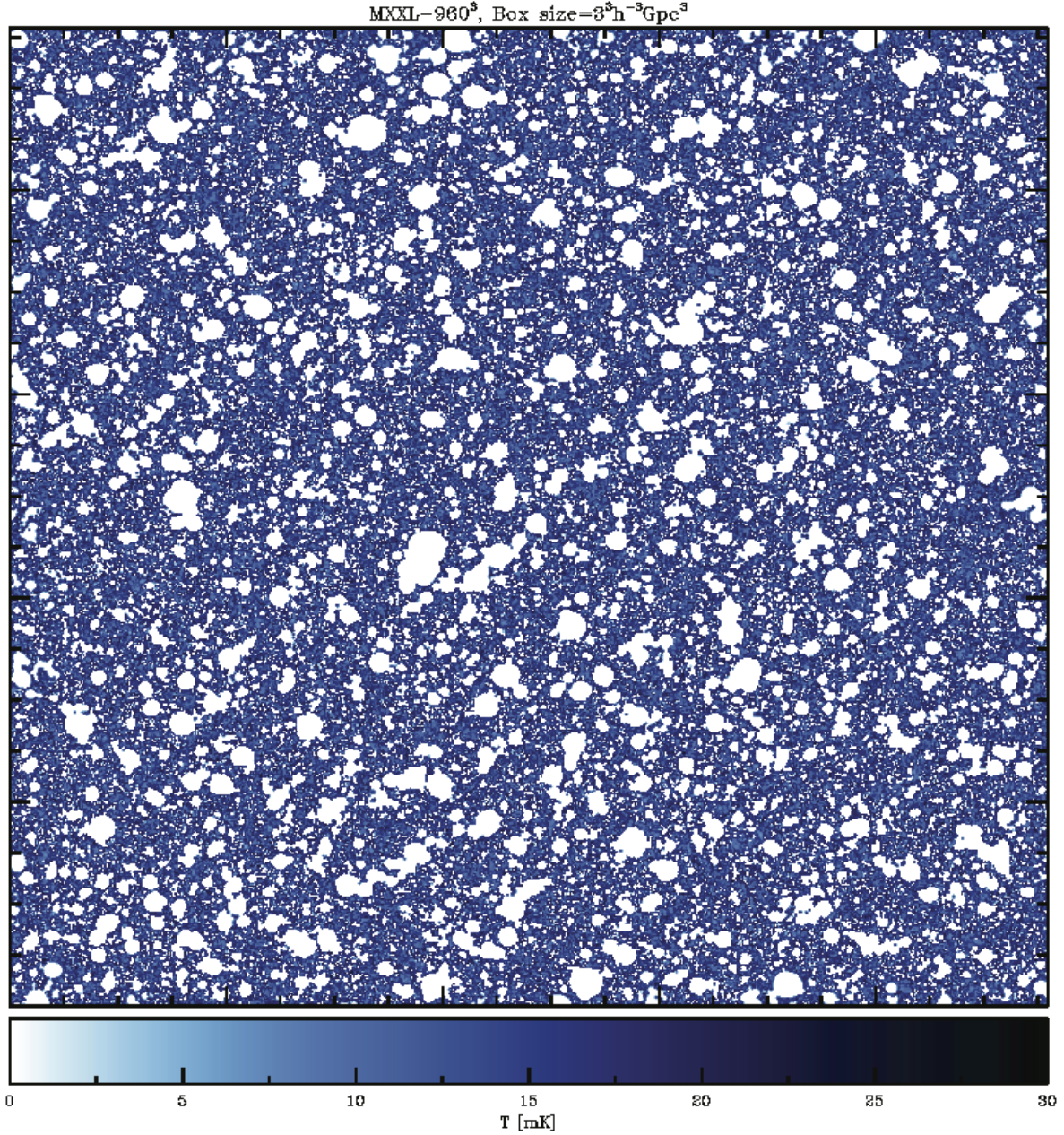


Figure 10. The 21-cm intensity map of the MXXL-960³ simulation which has a box size of 3000Mpc/h at $z \sim 7.272$ ($\langle x_i \rangle \sim 0.55$) with cell size 3.125Mpc/h. The slice is 3.125Mpc/h deep.

observations we modify the parameter in the Bow06 model which specifies the ratio between the sum of the mass in visible stars and brown dwarfs, and the mass in visible stars. This parameter (Υ) quantifies the assumption for the IMF of brown dwarfs ($m < 0.1M_\odot$) which contribute mass but no light to stellar populations. We adopt a value of $\Upsilon=4$ for the NOSN and NOSN (no suppression) models. More details on these models are provided in Kim et al. (2013). Note that the generated Q_{cell} values used in the large volume simulations for each of the models in Table 4 were calculated based on the Millennium-II dark matter simulation merger trees.

In each case we computed the 21cm power spectrum and plot the progression of a model in the parameter space of 21cm power spectrum amplitude and slope (note that since the ionized hydrogen fraction is not a direct observable). These curves are shown for the four models in Fig. 13, for wavenumbers $k_p=0.2$ (top) and $0.4h/\text{Mpc}$ (bottom). We also include arrows which show the direction from high to low expected mean global mass averaged neutral hydrogen fraction, $\langle x_{\text{HI}} \rangle$ (from $\langle x_{\text{HI}} \rangle = 0.944$ to 0.25; i.e., $z=9.278$ to 6.712). We see that the tracks separate into different parts

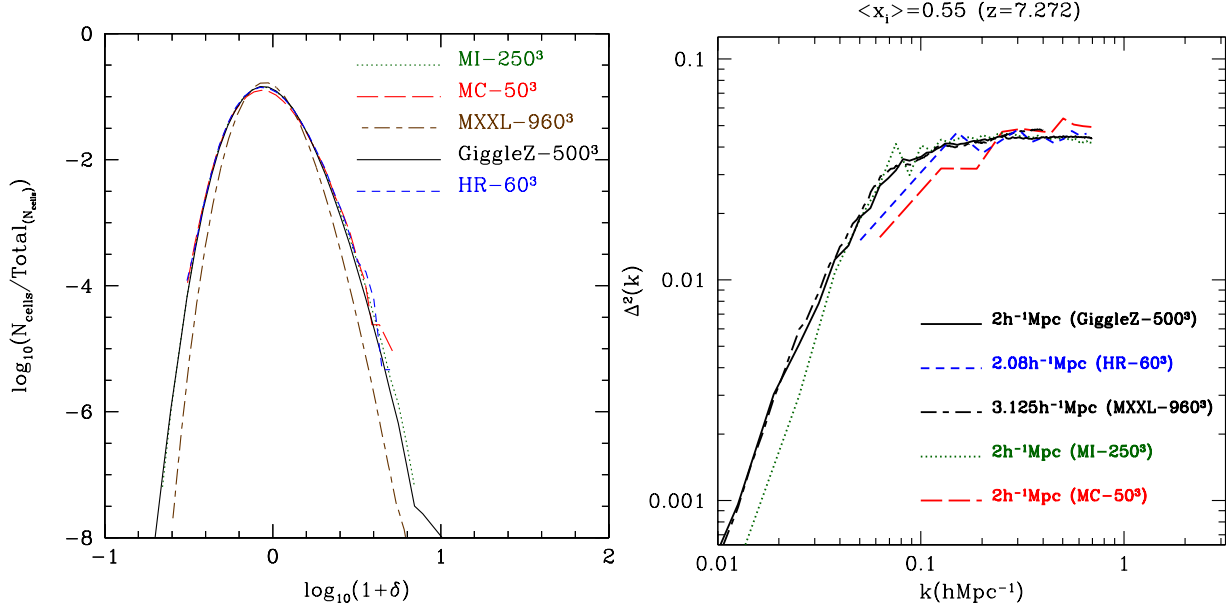


Figure 12. The left panel show the number of cells as a function of dark matter overdensity and redshifted 21-cm power spectra from the set of MC-50³, MI-250³ (2Mpc/h cell size), and MXXL-960³ (3.125Mpc/h cell size) models together with the set of HR-60³ (2.08Mpc/h cell size) and GiggleZ-500³ (2Mpc/h cell size) simulations. The right panel shows redshifted 21-cm power spectra of the models. Note that we plot rescaled dark matter number density distribution as described in §3

Table 4. The values of selected parameters which are different in the models. The columns are as follows: (1) the name of the model, (2) the value of the photoionization parameter V_{cut} (the suppression of cooling occurs by the photoionisation feedback when the host halo's circular velocity lies below a threshold value, V_{cut}), (3) the SNe feedback parameter, V_{hot} , (4) the IMF of brown dwarfs Υ (brown dwarfs contribute mass but no light to stellar population), and (5) comments giving model source or key differences from published models.

	$V_{\text{cut}}[\text{kms}^{-1}]$	$V_{\text{hot}}[\text{kms}^{-1}]$	Υ	Comments
Bow06	30	485	1	Bower et al. (2006), V_{cut} value change
Lagos11	30	485	1	Lagos et al. (2012)
NOSN	30	0	4	Bower et al. (2006), No SNe feedback
NOSN(no suppression)	0	0	4	Bower et al. (2006) No SNe feedback and No photoionization feedback

of the plain, primarily according to whether SN feedback is included or not (Bow06 and NOSN($V_{\text{cut}}=30\text{km/s}$))

The regulation of star formation and cooling of hot gas in small galaxies by the SNe feedback process leads to massive galaxies which are more biased towards dense regions, dominating the production of ionizing photons. As a result, the amplitude of the redshifted 21cm power spectrum from the Bow06 model is larger than the NOSN ($V_{\text{cut}}=30\text{km/s}$) model. There are also small differences from the form of the star formation law (Bow06 and Lagos11). This is because the modified star formation law in the Lagos11 model relative to the Bow06 model leads to different predictions for the number of luminous galaxies, and hence the clustering of the ionizing source population. There are further small differences according to whether photoionisation feedback is included or not [NOSN($V_{\text{cut}}=30\text{km/s}$) and NOSN(no suppression)]. The NOSN($V_{\text{cut}}=30\text{km/s}$) model has a larger amplitude for the 21-cm power spectrum than does the NOSN(no suppression) model because the photoionisation feedback effect in the absence of SNe feedback leads to more biased ionizing sources, so that the clustering amplitude increases. Note

that we do not include a model which has SNe feedback but no photoionization feedback, because there is very little effect from photoionisation feedback in models which have SNe feedback (Kim et al. 2013). Fig. 13 demonstrates that the power spectrum can be used to probe galaxy formation during reionization because the loci of the models fall in different parts of the parameter space of these observables.

5 SUMMARY AND CONCLUSIONS

The ionization structure of the IGM during reionization, and hence the observed 21-cm power spectrum, will be sensitive to the astrophysical properties of the reionizing galaxies. Theoretical models which aim to describe reionization are challenged by the very large range of spatial scales involved. In particular, to understand and predict upcoming observations that come from the new generation of wide field telescopes, MWA, LOFAR, PAPER and SKA, large volume reionization simulations which cover an area comparable to or in excess of the field of view of telescope will be required.

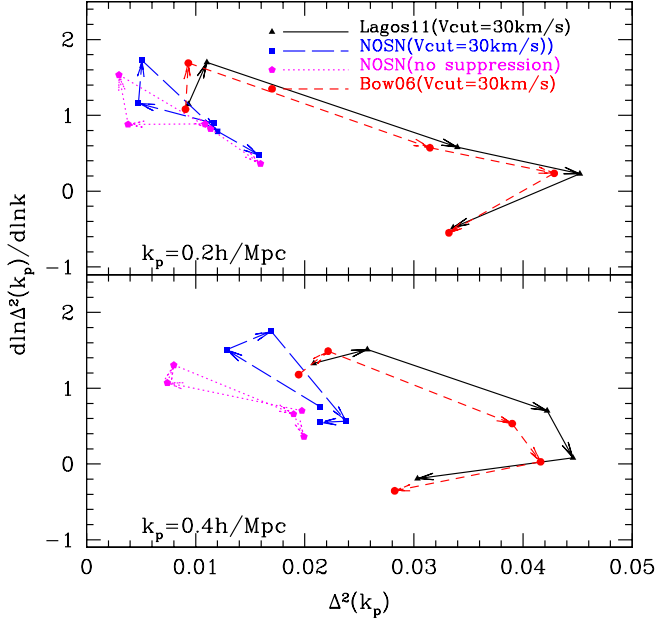


Figure 13. Plots show how the 21cm power spectrum changes using the loci of points in the parameter space of 21cm power spectrum amplitude and slope. Loci are shown for each of Lagos11 (our default model) (triangles, black solid line), NOSN(no suppression) (pentagons, violet dotted line), NOSN($V_{\text{cut}}=30\text{km/s}$) (squares, blue long dashed line), NOSN (no suppression) (octagons, green dot dashed line) and Bow06 (circles, red dashed line) models within the Millennium simulation. Results are shown for two central wavenumbers, $k_p = 0.2h/\text{Mpc}$ (top) and $0.4h/\text{Mpc}$ (bottom), corresponding to the point on the power spectrum where we measure the amplitude and slope. Arrows show the direction from high to low expected mean global mass averaged neutral hydrogen fraction, $\langle x_{\text{HI}} \rangle$

To address this problem, we extend the method described in Kim et al. (2013) which connects galaxy formation and reionization using high resolution but relatively small volume N-body simulations. To calculate ionization structure in large volume simulations we use the relation between the distribution of ionisation fraction and dark matter overdensity to generate reionization maps within the Millennium, MXXL and GigglesZ-main simulations.

We find that the amplitude of the redshifted 21-cm power spectra on large scales increases with simulation volume up to volumes of $(500\text{Mpc}/h)^3$ for $k < 0.1h/\text{Mpc}$. The power spectra are converged at still larger scales. This implies that modelling within 0.5Gpc volumes will be sufficient for interpretation of forthcoming observes of the 21-cm power spectrum from reionization $\sim \langle x_i \rangle = 0.55$. However since larger bubbles form in the highly ionized stage of reionization, we may need even larger volume simulations to see the convergence of the predicted 21cm power spectrum during the later stages of reionization $\langle x_i \rangle > 0.55$.

We apply our simulations to explore the sensitivity of the 21cm power spectrum to the physics of galaxy formation. We find that measurements of the amplitude and slope of the 21-cm power spectrum will be able to determine the level at which SN feedback operated in high-redshift galaxies. Our method could be applied to any model of reionization which has high resolution and sophisticated galaxy

formation physics, but small volume, in order to interpret a large scale redshifted 21cm power spectra from upcoming observations.

Acknowledgments HSK is supported by a Discovery Early Career Researcher Awards from the Australian Research Council (DE140100940). The Centre for All-sky Astrophysics is an Australian Research Council Centre of Excellence, funded by grant CE110001020. CMB acknowledges receipt of a Research Fellowship from the Leverhulme Trust. This work was supported in part by the Science and Technology Facilities Council rolling grant to the ICC. The Millennium, Millennium II, and Millennium-MXXL Simulations were carried out by the Virgo Consortium at the supercomputer centre of the Max Planck Society in Garching. Calculations for this paper were partly performed on the ICC Cosmology Machine, which is part of the DiRAC Facility jointly funded by STFC, the Large Facilities Capital Fund of BIS, and Durham University.

REFERENCES

- Ahn K., Iliev I. T., Shapiro P. R., Mellema G., Koda J., Mao Y., 2012, *ApJL*, 756, L16
- Angulo R. E., Springel V., White S. D. M., Jenkins A., Baugh C. M., Frenk C. S., 2012, *MNRAS*, 426, 2046
- Barkana R., Loeb A., 2001, *Phys. Rep.*, 349, 125
- Battaglia N., Natarajan A., Trac H., Cen R., Loeb A., 2013, *ApJ*, 776, 83
- Battaglia N., Trac H., Cen R., Loeb A., 2013, *ApJ*, 776, 81
- Baugh C. M., 2006, *Reports on Progress in Physics*, 69, 3101
- Bower R. G., Benson A. J., Malbon R., Helly J. C., Frenk C. S., Baugh C. M., Cole S., Lacey C. G., 2006, *MNRAS*, 370, 645
- Boylan-Kolchin M., Springel V., White S. D. M., Jenkins A., Lemson G., 2009, *MNRAS*, 398, 1150
- Ciardi B., Stoehr F., White S. D. M., 2003, *MNRAS*, 343, 1101
- Cole S., Lacey C. G., Baugh C. M., Frenk C. S., 2000, *MNRAS*, 319, 168
- Cui W., Liu L., Yang X., Wang Y., Feng L., Springel V., 2008, *ApJ*, 687, 738
- Dijkstra M., Haiman Z., Rees M. J., Weinberg D. H., 2004, *ApJ*, 601, 666
- Furlanetto S. R., Zaldarriaga M., Hernquist L., 2004a, *ApJ*, 613, 16
- Furlanetto S. R., Zaldarriaga M., Hernquist L., 2004b, *ApJ*, 613, 1
- Geil P. M., Wyithe J. S. B., 2008, *MNRAS*, 386, 1683
- Genel S., Vogelsberger M., Springel V., Sijacki D., Nelson D., Snyder G., Rodriguez-Gomez V., Torrey P., Hernquist L., 2014, *MNRAS*, 445, 175
- Gnedin N. Y., 2014, *ArXiv e-prints*
- Gnedin N. Y., Kravtsov A. V., Chen H.-W., 2007, *ArXiv e-prints*, 707
- Iliev I. T., Mellema G., Ahn K., Shapiro P. R., Mao Y., Pen U.-L., 2013, *ArXiv e-prints*
- Iliev I. T., Mellema G., Shapiro P. R., Pen U.-L., 2007, *MNRAS*, 376, 534

- Inoue A. K., Iwata I., Deharveng J.-M., 2006, MNRAS, 371, L1
- Jiang L., Helly J. C., Cole S., Frenk C. S., 2014, MNRAS, 440, 2115
- Kim H.-S., Baugh C. M., Benson A. J., Cole S., Frenk C. S., Lacey C. G., Power C., Schneider M., 2011, MNRAS, 414, 2367
- Kim H.-S., Lacey C. G., Cole S., Baugh C. M., Frenk C. S., Efstathiou G., 2012, MNRAS, 425, 2674
- Kim H.-S., Power C., Baugh C. M., Wyithe J. S. B., Lacey C. G., Lagos C. D. P., Frenk C. S., 2013, MNRAS, 428, 3366
- Kim H.-S., Wyithe J. S. B., Park J., Lacey C. G., 2013, MNRAS, 433, 2476
- Kim H.-S., Wyithe J. S. B., Power C., Park J., Lagos C. d. P., Baugh C. M., 2015, ArXiv e-prints
- Kim H.-S., Wyithe J. S. B., Raskutti S., Lacey C. G., Helly J. C., 2013, MNRAS, 428, 2467
- Kuhlen M., Faucher-Giguère C.-A., 2012, MNRAS, 423, 862
- Lagos C. d. P., Bayet E., Baugh C. M., Lacey C. G., Bell T. A., Fanidakis N., Geach J. E., 2012, MNRAS, 426, 2142
- Lidz A., Zahn O., McQuinn M., Zaldarriaga M., Hernquist L., 2008, ApJ, 680, 962
- McQuinn M., Lidz A., Zahn O., Dutta S., Hernquist L., Zaldarriaga M., 2007, MNRAS, 377, 1043
- Mesinger A., Dijkstra M., 2008, MNRAS, 390, 1071
- Mesinger A., Furlanetto S., 2007, ApJ, 669, 663
- Mesinger A., Furlanetto S., Cen R., 2011, MNRAS, 411, 955
- Norman M. L., Reynolds D. R., So G. C., Harkness R. P., 2013, ArXiv e-prints
- Pen U.-L., Staveley-Smith L., Peterson J. B., Chang T.-C., 2009, MNRAS, 394, L6
- Poole G. B., Blake C., Marin F. A., Power C., Mutch S. J., Croton D. J., Colless M., Couch W., Drinkwater M. J., Glazebrook K., 2014, ArXiv e-prints
- Santos M. G., Amblard A., Pritchard J., Trac H., Cen R., Cooray A., 2008, ApJ, 689, 1
- Santos M. G., Ferramacho L., Silva M. B., Amblard A., Cooray A., 2010, MNRAS, 406, 2421
- Springel V., White S. D. M., Jenkins A., Frenk C. S., Yoshida N., Gao L., Navarro J., Thacker R., Croton D., Helly J., Peacock J. A., Cole S., Thomas P., Couchman H., Evrard A., Colberg J., Pearce F., 2005, *Nature*, 435, 629
- Thomas R. M., Zaroubi S., Ciardi B., Pawlik A. H., Labropoulos P., Jelić V., Bernardi G., Brentjens M. A., de Bruyn A. G., Harker G. J. A., Koopmans L. V. E., Mellema G., Pandey V. N., Schaye J., Yatawatta S., 2009, MNRAS, 393, 32
- Trac H., Cen R., Loeb A., 2008, ApJL, 689, L81
- Wise J. H., Cen R., 2009, ApJ, 693, 984
- Wyithe J. S. B., Loeb A., 2013, MNRAS, 428, 2741
- Wyithe J. S. B., Morales M. F., 2007, MNRAS, 379, 1647
- Yajima H., Choi J.-H., Nagamine K., 2011, MNRAS, 412, 411
- Zahn O., Lidz A., McQuinn M., Dutta S., Hernquist L., Zaldarriaga M., Furlanetto S. R., 2007, ApJ, 654, 12